

Generating synthetic as-built additive manufacturing surface topography using progressive growing generative adversarial networks

Junhyeon SEO¹, Prahalada RAO², Bart RAEYMAEKERS^{1,*}

¹ Department of Mechanical Engineering, Virginia Tech, Blacksburg, VA 24061, USA

² Grado Department of Industrial and Systems Engineering, Virginia Tech, Blacksburg, VA 24061, USA

Received: 28 June 2023 / Revised: 25 August 2023 / Accepted: 15 September 2023

© The author(s) 2023.

Abstract: Numerically generating synthetic surface topography that closely resembles the features and characteristics of experimental surface topography measurements reduces the need to perform these intricate and costly measurements. However, existing algorithms to numerically generated surface topography are not well-suited to create the specific characteristics and geometric features of as-built surfaces that result from laser powder bed fusion (LPBF), such as partially melted metal particles, porosity, laser scan lines, and balling. Thus, we present a method to generate synthetic as-built LPBF surface topography maps using a progressively growing generative adversarial network. We qualitatively and quantitatively demonstrate good agreement between synthetic and experimental as-built LPBF surface topography maps using areal and deterministic surface topography parameters, radially averaged power spectral density, and material ratio curves. The ability to accurately generate synthetic as-built LPBF surface topography maps reduces the experimental burden of performing a large number of surface topography measurements. Furthermore, it facilitates combining experimental measurements with synthetic surface topography maps to create large data-sets that facilitate, e.g. relating as-built surface topography to LPBF process parameters, or implementing digital surface twins to monitor complex end-use LPBF parts, amongst other applications.

Keywords: additive manufacturing; surface topography; synthetic surface topography; generative adversarial networks

1 Introduction

Laser powder bed fusion (LPBF) is a metal additive manufacturing (AM) technology that uses a laser to selectively melt and fuse metal powder particles to manufacture three-dimensional (3D) free-form metal parts in a layer-by-layer fashion [1]. The process enables manufacturing parts with complex internal and external geometry that are difficult, if not impossible to make with traditional subtractive and formative manufacturing processes. The ability to transcend design and processing barriers, introduce novel alloys, reduce waste, shorten lead times, and

the potential for mass customization are attractive for, e.g. aerospace [2–4], automotive [5, 6], and biomedical [7–9] applications. However, surface topography is a critical determinant of functional properties, and thus LPBF parts often require post-processing to modify their structure and as-built surface topography prior to use in engineering applications. Post-processing techniques such as machining and superfinishing modify the surface topography of the as-built LPBF parts by removing material [10]. Additionally, heat treatments such as hot isostatic pressing [11, 12] and annealing [13] reduce porosity [14] and surface roughness [15]. Chemical treatment [16, 17] removes

* Corresponding author: Bart RAEYMAEKERS, E-mail: bart.raeymaekers@vt.edu.

partially melted metal powder particles from the as-built surfaces, and mechanical treatment such as shot peening modifies surface topography through mechanical impact [18, 19]. However, post-processing is time-consuming and costly. Moreover, limited accessibility of intricate internal or fine part geometry features, such as lattices, restricts post-processing of the as-built surfaces.

Hence, the ability to manufacture LPBF parts with a specific surface topography, without post-processing, could reduce manufacturing time and cost, and thus drive the adoption of LPBF as a viable production process for large quantities of parts with complex geometry. Consequently, researchers have attempted to relate the surface topography measurements of as-built surfaces to the LPBF process parameters. For instance, Özel et al. [20] used an artificial neural network (ANN) to derive the relationship between the LPBF laser power and the resulting as-built surface topography parameters, including areal surface topography parameters S_{ar} , S_{qr} , S_{skr} , and S_{ku} [21, 22]. Similarly, Detwiler et al. [23] employed multivariate regression, and Detwiler and Raeymaekers [24] used several interpretable and non-interpretable machine learning (ML) algorithms to derive data-driven models that relate the as-built surface topography to the corresponding LPBF process parameters. They showed that deterministic surface topography parameters, including asperity density, standard deviation of asperity heights, and mean asperity radius, correlate more closely with the LPBF process parameters than the commonly used areal surface topography parameters [21, 22].

Furthermore, the mechanical properties of LPBF parts, including fatigue life, also depend on the surface topography, because fatigue failure typically originates from a (sub)surface defect [25–27]. Thus, creating a digital twin of the as-built surface topography of the LPBF part would enable simulating the propagation of surface defects, voids, and cracks, to ultimately predict fatigue failure, and subsequently inform preventive maintenance or part replacement. Such digital condition monitoring is particularly useful for costly LPBF parts in critical engineering applications or assemblies.

These examples illustrate that obtaining accurate surface topography data is paramount to both deriving

data-driven models that relate the surface topography parameters of the as-built surface to the LPBF process parameters, and to implement digital twins of the as-built surface topography for, e.g. condition monitoring of high-value parts. Yet, performing these intricate surface topography measurements is time-consuming and requires trained personnel to operate sophisticated equipment and instrumentation [28, 29]. Thus, to reduce the need for costly surface topography measurements, one may supplement experimental surface topography data with numerically generated, synthetic data that comprises the same geometric features and statistical properties as the experimental data.

Accordingly, several mathematical techniques exist to numerically generate surface topography [30]. The random surface approach involves creating a surface topography map with random surface heights based on fractal or non-fractal methods and is often used to simulate engineering surfaces that result from specific machining operations [31–34]. The deterministic surface approach uses an algorithm that replicates specific surface characteristics, such as a topography pattern or texture feature [35–37]. Finally, the mixed surface approach combines elements of both techniques to generate surface topography with both random and deterministic features [38]. However, these existing approaches to numerically create surface topography are not well-suited to include the specific characteristics and geometric features of as-built LPBF surfaces, such as partially melted metal particles, porosity, laser scan lines, and balling that result from melt pool dynamics during the LPBF process [39, 40].

As a result, numerically generating surface topography that accurately represents as-built LPBF surfaces remains a significant challenge. Thus, the objective of this work is to derive a numerical model to generate synthetic surface topography that accurately replicates the specific geometric features and characteristics of as-built LPBF surfaces. We address this problem by using deep-learning ML algorithms, including the generative adversarial network (GAN) [41] and, specifically, the progressive growing GAN (PGGAN) [42].

A GAN comprises two neural networks: a generator network that creates synthetic surface topography maps, and a discriminator network that evaluates the

authenticity of the synthetic surface topography maps by comparing it to experimental surface topography measurements. These two networks are trained simultaneously, with the generator network trying to create increasingly realistic data that can mislead the discriminator network, and the discriminator network trying to accurately distinguish between the synthetic and authentic surface topography maps. Once trained, the generator network can accurately generate synthetic surface topography maps similar to the experimental surface topography maps.

We quantitatively evaluate the similarity between synthetic and experimental surface topography maps using areal and deterministic surface topography parameters, power spectral density, and material ratio curves [23]. We note that Eastwood et al. [43] recently also documented using a PGGAN to create synthetic surface topography maps that result from electron beam powder bed fusion (EBPBF). However, they only used areal surface topography parameters to characterize their surface topography, and even concluded that hybrid surface topography parameters could be more appropriate.

The ability to generate synthetic surface topography maps with the same geometric features and characteristics as experimental surface topography maps reduces the need for resource-intensive experimental data collection, and it simultaneously augments data volume and diversity. Hence, the outcomes of this work support the creation of data-driven models and digital twin models, including the process–structure–surface topography relationship, a topic of importance that remains inadequately understood for developing LPBF parts as functional end-use components.

2 Materials and methods

2.1 Additive manufacturing of specimens

We use a 3D Systems ProX SMP 320 LPBF printer to manufacture dogbone specimens with recycled 40 μm Inconel 718 (IN718) powder. The six specimens used in this work are a sub-set of the specimens we have used in previous studies [23, 24, 26, 44]; we include a summary of the LPBF process parameters in Appendix A. Figure 1 schematically shows the layout

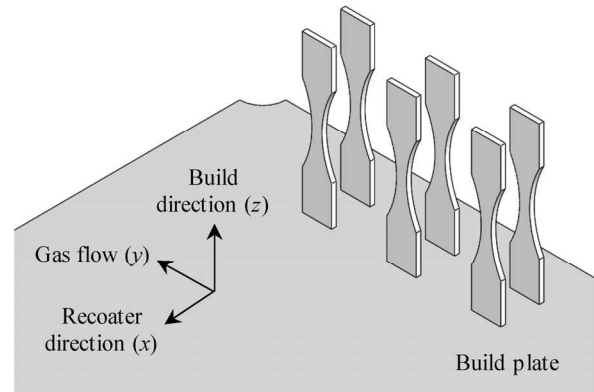


Fig. 1 Layout of the dogbone specimens on the build plate, relative to LPBF process directions.

of the dogbone specimens on the build plate, and illustrates their geometry and build orientation relative to the build, re-coater, and gas flow directions. The re-coater distributes a uniform layer of metal powder prior to selectively fusing the contours and geometric features of each layer of the LPBF part, whereas the gas flow evacuates smoke from the build volume to maintain a clear optical path between the laser and the build plate.

2.2 Measurement of as-built surface topography

We measure the as-built surface topography of each specimen using an Olympus LEXT OLS 5000 confocal laser scanning microscope (CLSM) with a 20 \times lens, which results in a 1.8 mm \times 1.8 mm field-of-view, with a lateral and vertical resolution of 0.625 μm and 0.006 μm , respectively. These parameters result from a convergence study to ensure that the surface topography parameters derived from the surface topography measurements are almost independent of the field-of-view and resolution. Surface topography measurements quantify the surface height z as a function of discrete coordinate locations on the surface, i.e., $z = f(x, y)$, from which we derive surface topography parameters to describe the surface characteristics. We correct the surface topography measurements for specimen tilt and set the centerline average to zero. Figure 2 shows a schematic of a dogbone specimen geometry, and identifies the six surface topography measurement locations (three on each side of the specimen). We show a typical surface topography measurement, with several magnified inset images A, B, and C, to illustrate common

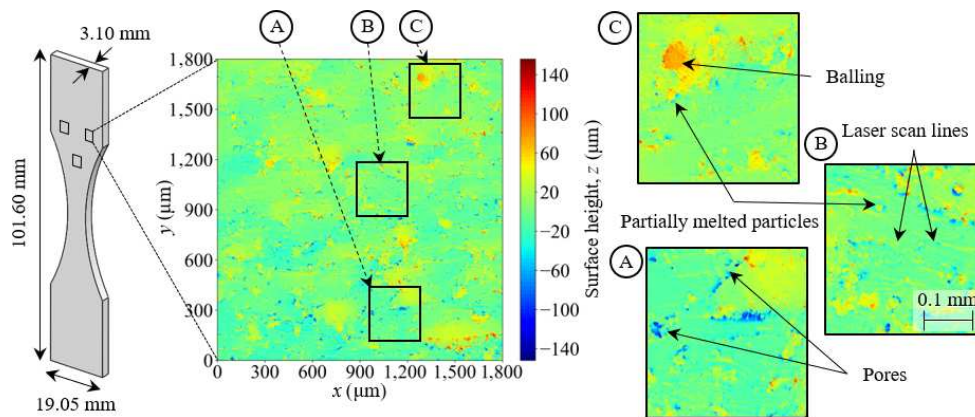


Fig. 2 Dogbone specimen geometry and typical as-built surface topography map with magnified inset images that illustrate distinct LPBF surface features, showing pores, “balling”, partially melted powder particles, and laser scan lines.

characteristics and geometric features of the as-built LPBF surface topography [39, 40]. Pores result from incomplete fusion of the metal powder particles, which impacts the mechanical properties of the part [45–48]. Furthermore, in thin walls and edges of unsupported overhangs, such as the specimens used in this work, onset of melt pool instability often occurs. The melt pool length increases relative to its diameter and segregates into discrete chunks, which is often called “balling”. In turn, it impedes consolidation of the material, which results in a rough surface finish, and causes geometric inaccuracy [49]. Also, in parts with steep overhang features, partially melted powder particles adhere to the surface as a result of excessive heating [49]. Additionally, we observe laser scan lines in the surface topography map, which are an artifact of the LPBF process [50]. Finally, the layer-by-layer LPBF process relies on discrete steps in the build direction to create oblique or curved surfaces, which gives rise to the so-called “staircase effect”. However, the staircase effect is minimal in this work since we only consider side surfaces of vertically-oriented dogbone specimens [51, 52].

2.3 Generating synthetic surface topography

Figure 3 schematically illustrates the process of generating synthetic surface topography maps using the PGGAN model. It schematically shows sampling of the experimental surface topography maps to create an experimental dataset to train the PGGAN model (Fig. 3(a)), the architecture of the GAN (Fig. 3(b)) and PGGAN models (Fig. 3(c)), in addition to generating

synthetic surface topography maps using the optimized generator network that results from the trained PGGAN model (Fig. 3(d)). We employ the original PGGAN model without modifying its architecture. Hence, we refer the reader to Ref. [42] for a comprehensive mathematical description of the PGGAN model and its architecture, including the organization of convolutional layers, activation functions, and the number of hyperparameters. However, we briefly explain the concepts here, specifically in the context of generating synthetic surface topography maps. We also clarify that the PGGAN model in this work comprises more than 20 million hyperparameters, mainly due to the extensive set of large-sized convolutional layers and the convolutional process. Thus, it is not practical to present all hyperparameters here; instead, we make the trained models available via GitHub.

First, we create a dataset of experimental (authentic) surface topography maps to train the PGGAN model. We randomly sample $m = 500$, $512 \text{ pixels} \times 512 \text{ pixels}$ sub-sections of each experimental surface topography map (see Fig. 3(a)), which is a common image size in computer vision applications, and corresponds to a $320 \mu\text{m} \times 320 \mu\text{m}$ sub-area of the $1.8 \text{ mm} \times 1.8 \text{ mm}$ field-of-view of the experimental surface topography measurement. Thus, based on 6 specimens, 6 measurement locations per specimen, and $m = 500$ samples per measurement location, the training dataset comprises $6 \times 6 \times 500 = 18,000$ experimental surface topography maps. The maximum peak height S_p and valley depth S_v of the $512 \text{ pixels} \times 512 \text{ pixels}$

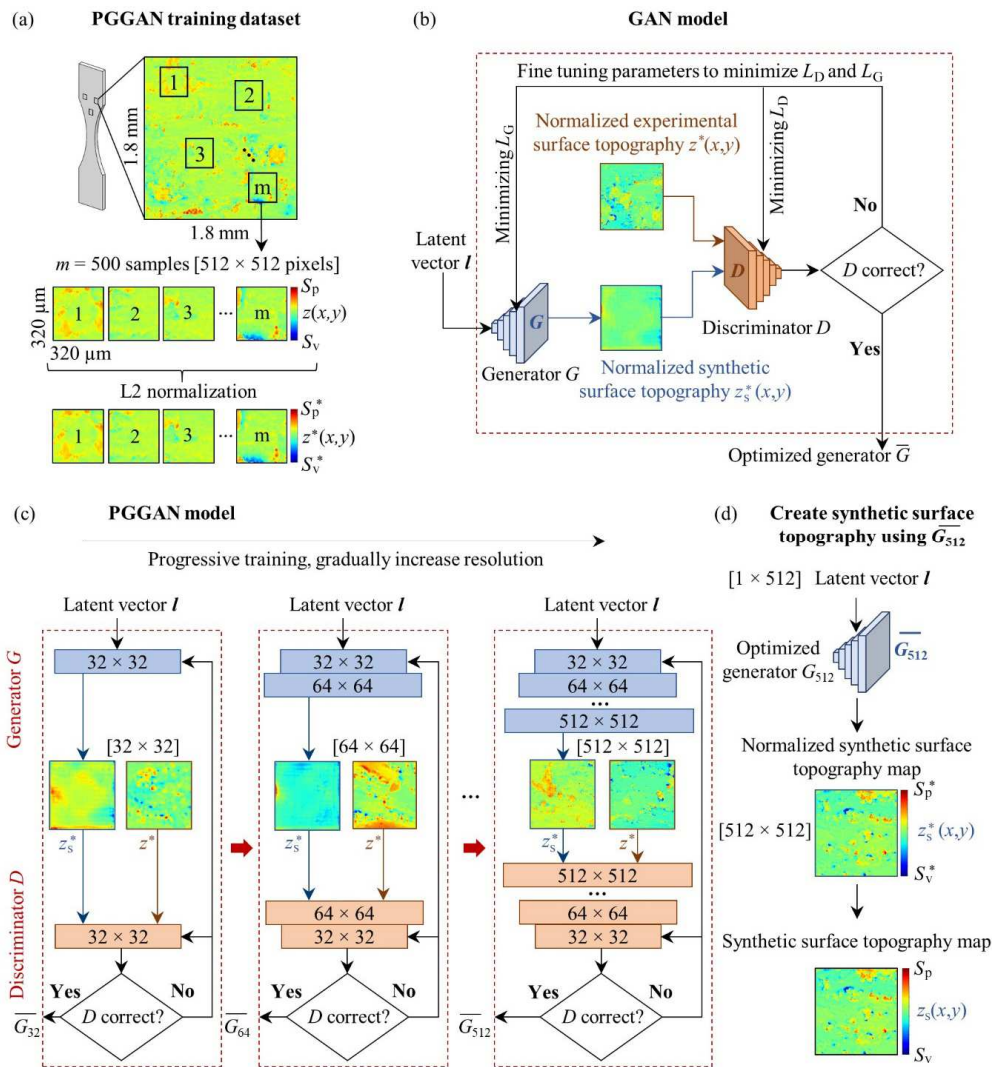


Fig. 3 Methodology to generate synthetic surface topography, similar to an experimental as-built LPBF surface topography measurement, showing (a) sampling the experimental dataset to train the PGGAN model, (b) architecture of the GAN model, (c) architecture of the PGGAN model that illustrates progressively increasing the resolution of the surface topography, and (d) using the optimized generator network to create synthetic surface topography maps.

experimental surface topography maps exhibit significant variability, as a result of the distinct geometric features of the as-built LPBF surface (see Fig. 2). Hence, we normalize the experimental surface topography maps $z(x, y)$ to $z^*(x, y)$ using the L2 norm (see Fig. 3(a)), because it is well-known that scale differences may lead to divergence and sub-optimal results when training the PGGAN model.

Figure 3(b) schematically depicts the architecture of the GAN model, which comprises a generator G and a discriminator D convolutional neural network (CNN) [42]. The generator converts a latent vector I , which contains random input values that follow a

standard normal distribution (mean 0 and standard deviation 1), into a normalized synthetic surface topography map $z_s^*(x, y)$. The generator gradually up-samples the input values using transposed convolutions to increase both the spatial dimensions and the complexity of the synthetic surface topography maps. To differentiate between synthetic and experimental surface topography maps, the discriminator uses convolution to first extract hierarchical, characteristic features of both the synthetic and all experimental surface topography maps it aims to replicate. Convolution involves applying filters to the surface topography to extract spatial patterns and

capture local relationships. Then, the discriminator estimates the probability of authenticity of the synthetic surface topography map by comparing the characteristics and geometric features to those of the experimental surface topography maps, ultimately producing a binary classification of authentic versus synthetic [41].

A feedback loop between the generator and discriminator establishes adversarial training, in which the discriminator provides feedback to the generator by evaluating the authenticity of its generated synthetic surface topography maps. Thus, it enables iterative refinement by fine-tuning the parameters (weights and biases) of the convolutional layers of both networks to minimize the GAN's loss function [41]. The loss function includes the generator loss L_G and the discriminator loss L_D . Here,

$$L_G = -\log(D(G(I))) \quad (1)$$

where $G(I) = z_s^*$ is the output of the generator based on the latent vector I , i.e., the normalized synthetic surface topography map. The output of the generator serves as input to the discriminator, which produces $D[G(I)]$ to determine whether $G(I) = z_s^*$ is authentic or synthetic. The discriminator loss is given as [41]:

$$L_D = -\log(D(G(z_s^*))) + \log(1 - D(G(z_s^*))) \quad (2)$$

We note that increasing the size of the latent vector increases the diversity of the synthetic surface topography maps that result from the generator, but also increases its computational cost. Hence, throughout this work, we use latent vectors of size 1×512 [42].

Figure 3(c) schematically illustrates the PGGAN model, which is an extension of the GAN model, specifically intended for high-resolution image data, such as surface topography maps. It uses the adversarial training concept of GANs (Fig. 3(b)), but in addition, it gradually increases the resolution of the generator and discriminator networks to avoid discontinuities in the synthetic surface topography maps that may occur when training a GAN directly on high-resolution data. Initially, the generator G_{32} and discriminator D_{32} operate on surface topography maps of 32 pixels \times 32 pixels to capture fundamental features of the experimental surface topography maps.

We obtain the experimental surface topography maps used in the adversarial training with gradually increasing resolution by down-sampling the 512 pixels \times 512 pixels experimental surface topography samples of Fig. 3(a). When the adversarial training of G_{32} and D_{32} reaches convergence, the model doubles the resolution of the surface topography maps to 64 pixels \times 64 pixels by adding convolutional layers to the generator G_{64} and discriminator D_{64} that match the new resolution of the surface topography maps. Here, convergence is defined as completing a minimum of 50 epochs (computer system time) in combination with reducing the change of the loss functions between successive iterations ΔL_G and $\Delta L_D < 10\%$. The adversarial training of G_{64} and D_{64} minimizes L_G and L_D , prior to doubling the resolution of the surface topography maps again. This process repeats until we reach G_{512} and D_{512} , which results in an optimized generator \bar{G}_{512} , capable of generating high-resolution synthetic surface topography maps of 512 pixels \times 512 pixels. The optimized generator is defined by the minimum L_G and L_D .

Note that to evaluate the convergence of the GAN model we only track and visualize L_G , because it directly addresses the quality of the synthetic surface topography maps, which is the primary objective of the PGGAN model in this work. Thus, focusing solely on the generator loss offers a concise depiction of the training process of the model in alignment with the foundational principles of the Nash equilibrium, which serves as the basis of the GAN's adversarial training process [41].

The computationally intensive nature of the PGGAN model necessitates GPU calculations for efficient training [42]. We use a high-performance computing (HPC) system based on an Nvidia A100 GPU 80 GB in the Advanced Research Computing (ARC) center at Virginia Tech, USA.

Finally, the optimized generator \bar{G}_{512} uses a latent vector I with random input values to create normalized synthetic surface topography maps $z_s^*(x, y)$ that are equivalent to the L2 normalized experimental surface topography maps (Fig. 3(d)). Different latent vectors generate multiple synthetic surface topography maps. Since we normalize the experimental surface topography maps, we must also linearly re-scale the

normalized synthetic surface topography maps $z_s^*(x, y)$ to dimensional synthetic surface topography maps $z_s(x, y)$. Hence,

$$z_s(x, y) = S_v + \frac{z_s^*(x, y) - S_v^*}{S_p^* - S_v^*} (S_p - S_v) \quad (3)$$

where S_p and S_v are randomly selected maximum peak height and valley depth values from the 18,000 experimental surface topography maps we use to train the PGGAN model. S_p^* and S_v^* are the normalized maximum peak height and valley depth values of the normalized synthetic surface topography map, which represent the maximum and minimum values of $z_s^*(x, y)$.

2.4 Similarity between the experimental and synthetic surface topography maps

We generate 1,000 synthetic surface topography maps $z_s(x, y)$ using each of the optimized generators, \bar{G}_{128} , \bar{G}_{256} , and \bar{G}_{512} , trained with the PGGAN model. We do not generate synthetic surface topography maps with a resolution of less than 128 pixels \times 128 pixels since they do not capture the distinct characteristics and geometric features of the LPBF surface topography (see Section 3). We compare areal and deterministic surface topography parameters of the synthetic surface topography maps $z_s(x, y)$ to those of 1,000 randomly selected experimental surface topography maps $z(x, y)$, and we quantify their similarity. For each surface topography parameter, we determine the minimum, maximum, mean, median, and the 25th and 75th percentiles.

Specifically, areal surface topography parameters include the average surface roughness S_a , the skewness S_{sk} , and the kurtosis S_{ku} [22], and deterministic surface topography parameters include the asperity density η , mean asperity radius R_s , and standard deviation of asperity heights σ_s . To determine the deterministic surface topography parameters, we first identify each peak i of the surface topography map using an 8-nearest neighbor scheme [53, 54]. The standard deviation of asperity heights σ_s derives directly from the peak heights, whereas the asperity density η results from the number of peaks and the nominal surface area of the surface topography measurement. The

curvature of each peak i in two orthogonal directions x and y is $\kappa_{x,i} = d^2z/dx^2$ and $\kappa_{y,i} = d^2z/dy^2$, and the radius of curvature ρ_i of that peak is the inverse of the average of its κ_x and κ_y , i.e., $\rho_i = -[(\kappa_{x,i} + \kappa_{y,i})/2]^{-1}$. The mean asperity radius R_s is the arithmetic mean of all individual peak radii. We use a central finite difference scheme to calculate the derivatives of the surface heights dz/dx and d^2z/dx^2 .

Additionally, to identify the differences between areal and deterministic topography parameters of the experimental and synthetic surface topography maps, we determine the radially averaged power spectral density (PSD) [55] and the material ratio curve M_r of selected surface topography maps, which offer a qualitative comparison between the experimental and synthetic surface topography [22].

3 Results and discussion

3.1 Adversarial training of the PGGAN model

Figure 4 illustrates the adversarial training process of the PGGAN model, depicting the generator loss L_G versus the computer system time (Epoch), and indicating the gradually increasing resolution from 32 pixels \times 32 pixels to 512 pixels \times 512 pixels with different colors. From Fig. 4, we observe that the number of epochs required to achieve convergence (at least 50 epochs, and $\Delta L_G < 10\%$ and $\Delta L_D < 10\%$ between successive iterations) increases with increasing resolution because the data volume increases, which adds complexity to the model and computation. We also observe from Fig. 4 that the variation of L_G increases with increasing resolution because it requires adding convolutional layers with increased resolution to the generator and discriminator networks in the PGGAN model (see Fig. 3(c)), which introduces new, unknown hyperparameters, such as weights and biases. As a result, L_G and L_D become arithmetically unstable, often necessitating further tuning to converge to a steady loss value. The magnified inset image in the convergence plot of Fig. 4 visualizes L_G for the GAN training at the highest resolution (512 pixels \times 512 pixels), spanning epochs 300 to 450. We perform Gaussian smoothing (red dashed line in the inset image) to emphasize the descending trend of L_G .

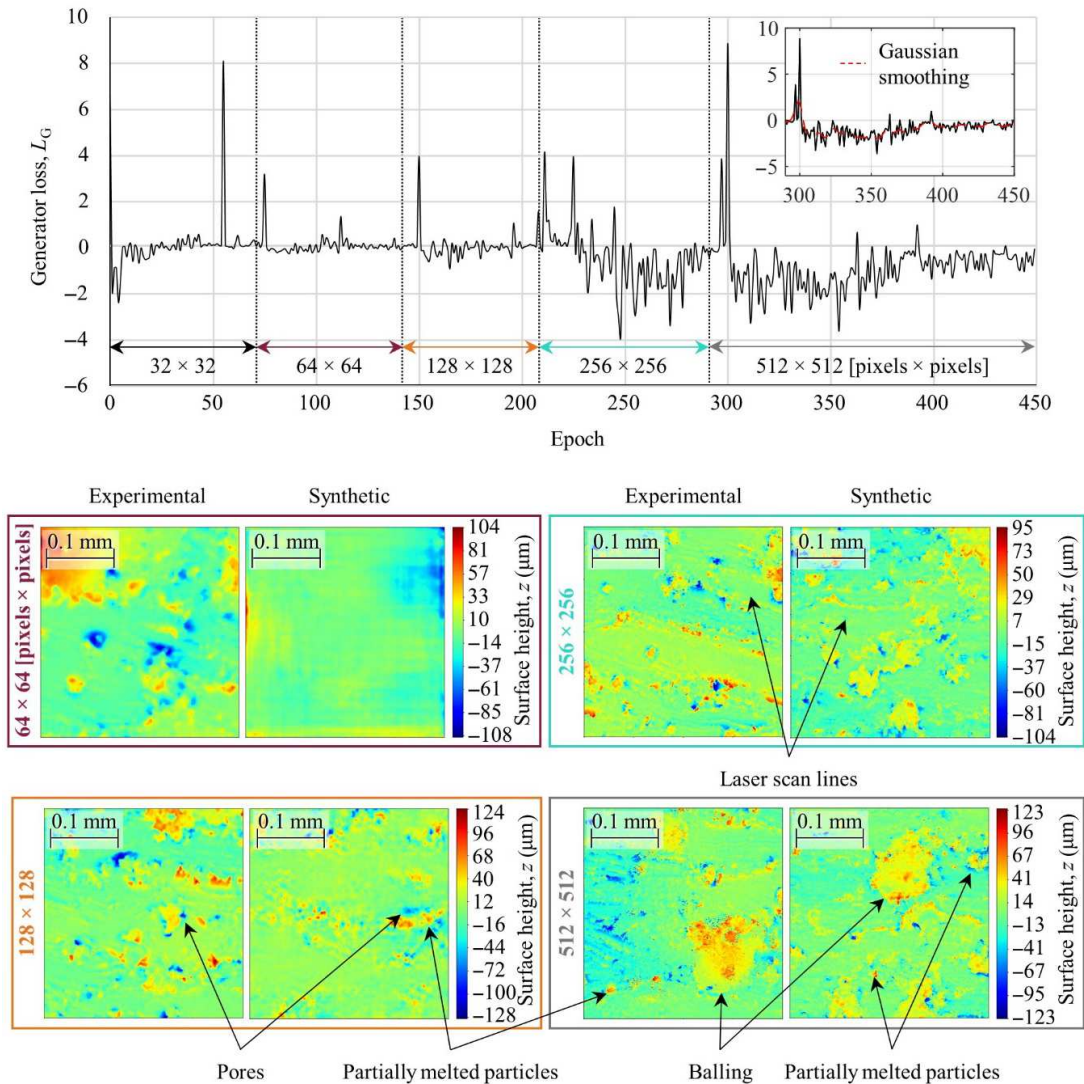


Fig. 4 Adversarial training of the PGGAN model showing the loss function versus the computer system time (Epoch) for gradually increasing resolution, with typical examples of experimental and synthetic surfaces for 64, 128, 256, and 512 pixels.

which also indicates the interaction between the generator and discriminator, and illustrates the inherent equilibrium convergence in GAN training.

Additionally, Fig. 4 shows typical examples of experimental (left) and synthetic (right) surface topography maps for each resolution (64, 128, 256, and 512 pixels). The synthetic surface topography maps replicate distinct as-built LPBF surface features and characteristics, including pores and un-melted particles, when the resolution reaches 128 pixels \times 128 pixels. Further increasing the resolution to 512 pixels \times 512 pixels, reveals additional features in the synthetic surface topography maps, such as laser scan patterns and balling.

3.2 Comparing the experimental and synthetic as-built surface topography maps

Figure 5 shows a comparison between the surface topography parameters that characterize the experimental and synthetic surface topography maps (see Section 2.4), as a function of surface topography map resolution, including the minimum and maximum (black error bars), mean (blue diamond), median (red line), 25th and 75th percentile (blue box), and outliers (red markers), for (a) S_{av} (b) S_{skv} (c) S_{kuv} and deterministic topography parameters (d) η , (e) R_s and (f) σ_s . We only show the results for surface topography maps with resolution of 128, 256, and

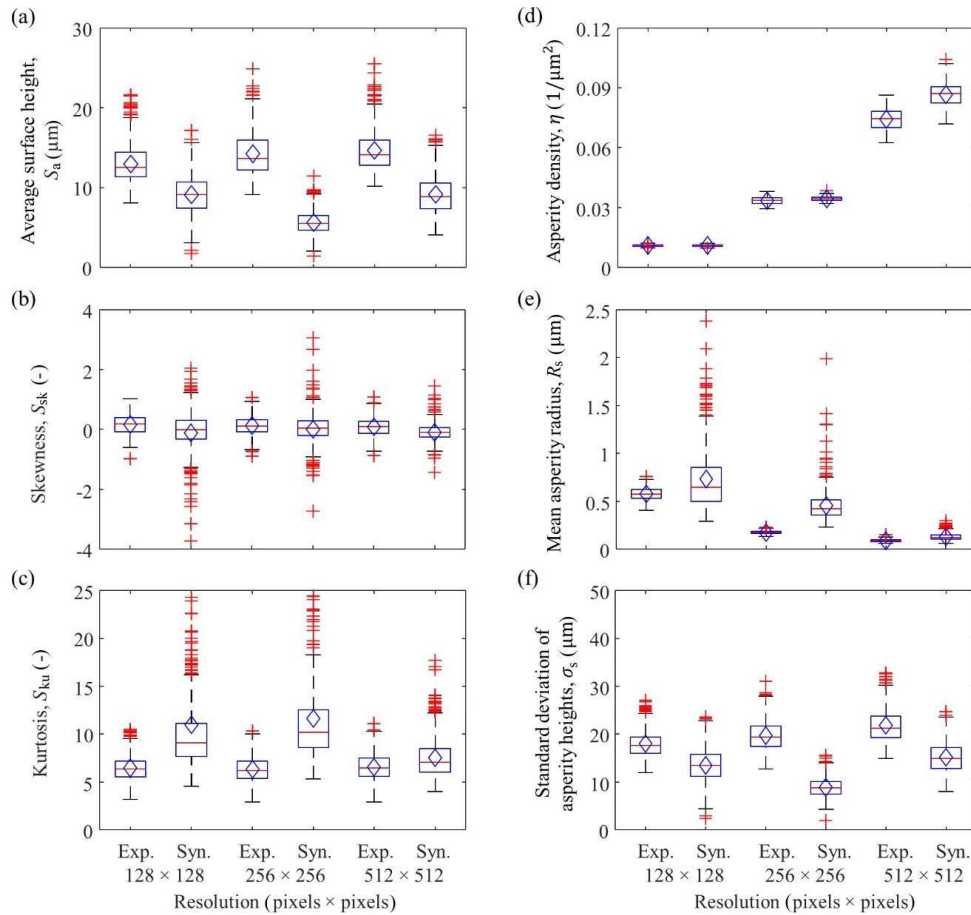


Fig. 5 Comparison between the surface topography parameters (a) S_a , (b) S_{sk} , (c) S_{ku} , (d) η , (e) R_s , and (f) σ_s , of the experimental and synthetic surface topography maps, as a function of resolution showing minimum, maximum (black error bars), mean (blue diamond), median (red line), 25th and 75th percentile (blue box), and outliers (red markers).

512 pixels \times 512 pixels, since surface topography maps with a resolution smaller than 128 pixels \times 128 pixels did not capture the distinct as-built LPBF surface topography characteristics and geometric features (see Fig. 2).

From Fig. 5(a), we observe that the synthetic compared to the experimental surface topography maps consistently show a lower S_a value, independent of the resolution. For instance, the median value of S_a is 34.7% lower for the synthetic than for the experimental surface topography maps with a resolution of 512 pixels \times 512 pixels. However, comparing the radially averaged PSD (see Fig. 6(a)) and material ratio curve M_r (see Fig. 6(b)) of selected synthetic and experimental surface topography maps shows that the synthetic surface topography maps underestimate the surface heights of the low-frequency components, and overestimate the surface heights of the high-

frequency components (Fig. 6(a)) compared to the experimental surface topography maps. The magnitudes of the low-frequency surface height variations dominate those of the high-frequency ones, which explains the difference between the median S_a value of synthetic and experimental surface topography maps. Additionally, the synthetic surface topography underestimates the height of the peaks and overestimates the depth of the valleys (Fig. 6(b)), which further contributes to a lower median S_a for the synthetic compared to the experimental surface topography maps.

From Figs. 5(b) and 5(c), we observe that the skewness S_{sk} and the kurtosis S_{ku} of the synthetic and experimental surface topography maps are in good agreement. $S_{sk} \approx 0$, which indicates that there is almost no bias between peaks and valleys. However, $S_{ku} \gg 3$ implies a “spikey” surface topography, which is also

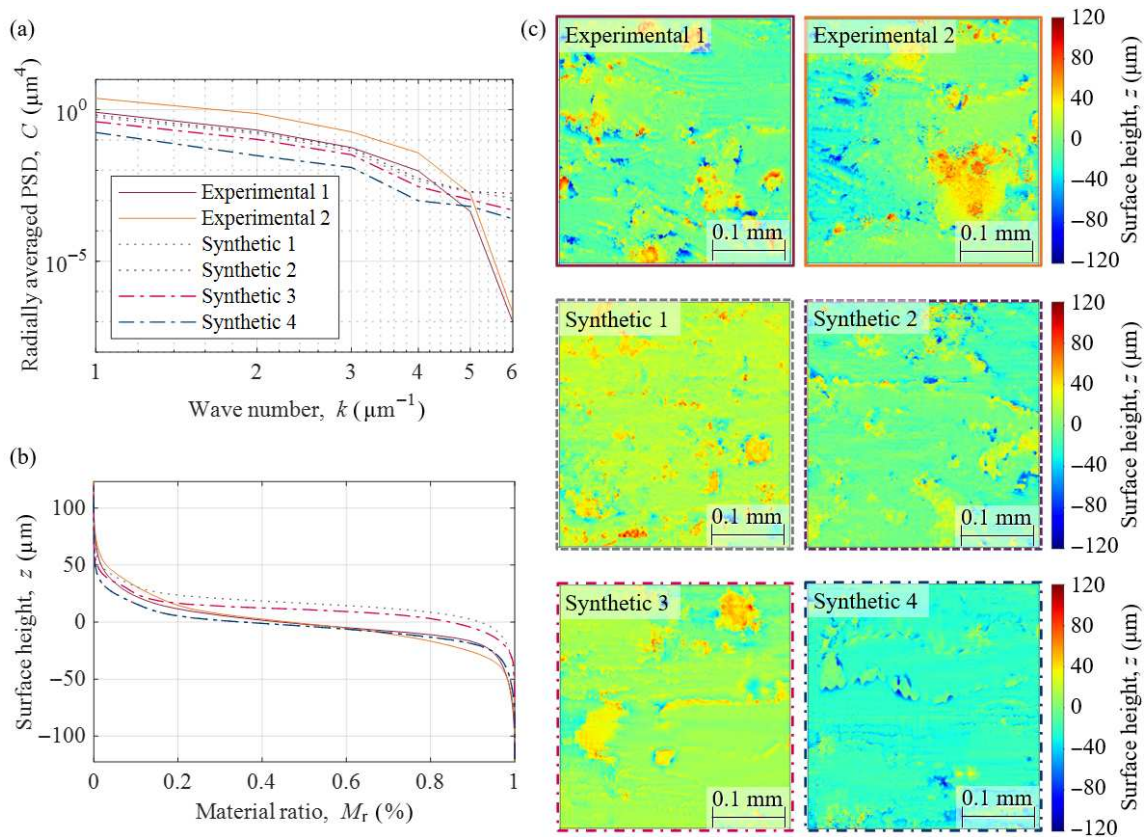


Fig. 6 Characteristics of experimental and synthetic surface topography maps, showing (a) radially averaged PSD, (b) material ratio curve, (c) for selected experimental and synthetic surface topography maps.

evident from the deterministic surface topography parameters $\sigma_s \gg R_s$. The recognition of “spiky” geometric features within the synthetic surface topography maps indicates that the PGGAN model replicates specific surface characteristics indicative of partially melted metal particles and laser scan lines, which are common sources of $S_{ku} \gg 3$. We also note that the kurtosis of the experimental surface topography maps is consistently lower than that of the synthetic surface topography maps, independent of the resolution, which we again explain based on the radially averaged PSD data (see Fig. 6(a)).

From Figs. 5(d), 5(e), and 5(f), we observe that the deterministic surface topography parameters calculated from the experimental and synthetic surface topography maps show fair agreement. Specifically, we determine a difference of 17%, 36%, and 29%, respectively, between the median values of the asperity density η , mean asperity radius R_a , and standard deviation of asperity heights σ_s of the synthetic and experimental 512 pixels \times 512 pixels surface topography maps. We

also observe that η increases and R_s decreases with increasing resolution, because the increased resolution enables resolving additional detail and features of the surface topography. Similar to the S_a values, σ_s is consistently lower for the synthetic compared to the authentic surface topography maps, independent of resolution, because the synthetic surface topography underestimates the magnitudes of the low-frequency variations of the surface topography.

Figure 6 shows (a) the radially averaged PSD [56] and (b) the material ratio M_r curves [22] of typical experimental and synthetic surface topography maps depicted in Fig. 6(c), which are representative of the dataset. From Fig. 6(a), we observe that the synthetic surface topography maps underestimate the magnitudes of the low-frequency ($k < 5$) variations, and overestimate the magnitudes of the high-frequency ($k \geq 5$) variations of the surface topography, as highlighted in the discussion of the results of S_a , S_{ku} , and σ_s . Note that $k = 2\pi/\lambda$ is the wave number and λ is the spatial wavelength of the surface topography. The material

ratio curves M_r (Fig. 6(b)) qualitatively show a high degree of similarity between the surface height distributions of the synthetic and experimental surface topography maps.

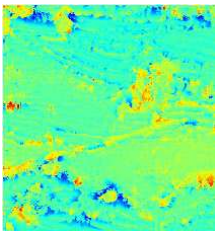
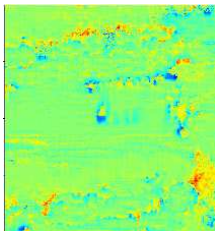
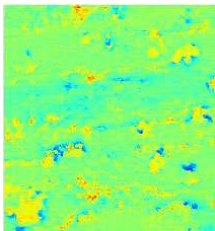
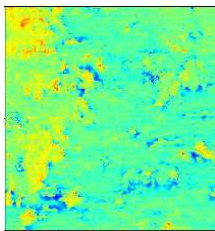
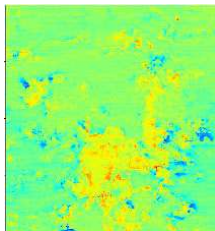
Figures 5 and 6 illustrate that on average, the synthetic and experimental surface topography maps show good agreement, based on the comparison of areal and deterministic surface topography parameters. However, substantial variation may exist between specific surface topography parameters of selected synthetic surfaces. This results from re-scaling the surface topography maps from its normalized $z_s^*(x, y)$ to its dimensional $z_s(x, y)$ form (see Section 2), using S_p and S_v values randomly selected from the 18,000 experimental surface topography maps. Even though randomly selecting S_p and S_v contributes to enhancing the diversity of synthetic surface topography maps, it falls short in creating the desired surface topography parameter values.

Thus, to illustrate creating synthetic surface topography maps with surface topography parameter values similar to those of the experimental surface topography maps, we randomly select four synthetic surface topography maps that visually represent the distinct characteristics and geometric features of the as-built LPBF surfaces, including partially melted

particles, pores, and laser scan lines, and we compare it to a randomly selected experimental surface. We re-scale the synthetic surface topography maps with S_p and S_v values identical to the experimental surface topography map. Table 1 presents a visual comparison of the four selected synthetic surface topography maps, typical of the entire dataset, and the corresponding experimental surface topography map, in addition to their areal and deterministic surface topography parameters. We indicate the percent difference between the parameters derived from the synthetic and experimental surface topography between parentheses.

From Table 1, we qualitatively observe close resemblance between the selected synthetic and experimental surface topography maps. Additionally, their S_a and S_q values are remarkably close and $S_{sk} \approx 0$, which indicates no bias between peaks and valleys. However, the S_{ku} values and deterministic parameters show substantially greater differences. Regardless, Fig. 5 shows that the 25th and 75th percentile boxes of the S_{sk} and deterministic surface topography parameters of both experimental and synthetic surface topography maps almost entirely overlap. Hence, the synthetic surfaces replicate the characteristics of the as-built LPBF surface topography even though they exhibit variations within a specific range.

Table 1 Qualitative and quantitative comparison between selected synthetic and experimental surface topography maps that show distinct LPBF surface topography features.

Parameters	Experimental	Synthetic			
		Surface 1	Surface 2	Surface 3	Surface 4
Surface contour					
S_a (μm)	16.379	17.318 (5.74 %)	15.667 (−4.34 %)	15.655 (−4.41 %)	18.391 (12.29 %)
S_q (μm)	22.529	21.690 (−3.72 %)	20.404 (−9.43 %)	21.778 (−3.33 %)	23.035 (2.25 %)
S_{sk}	0.187	0.224 (19.78 %)	0.283 (51.33 %)	−0.262 (40.11 %)	0.122 (−34.76 %)
S_{ku}	5.356	4.447 (−16.95 %)	4.288 (−19.93 %)	4.558 (−14.88 %)	3.386 (−36.76 %)
η ($1/\mu\text{m}^2$)	0.066	0.081 (22.83 %)	0.081 (23.04 %)	0.091 (38.31 %)	0.089 (35.72 %)
R_s (μm)	0.085	0.108 (22.76 %)	0.099 (16.91 %)	0.075 (−11.21 %)	0.094 (11.75 %)
σ_s (μm)	23.724	19.977 (−15.79 %)	18.772 (−20.87 %)	23.613 (−0.47 %)	19.792 (−16.57 %)

Consequently, the trained generator creates synthetic as-built LPBF surface topography maps that closely resemble the characteristics of the experimental data, while also introducing diversity and variability. Thus, the model generates new data points that have the same essential features as the original data but exhibit subtle variations, which effectively augments the dataset. Furthermore, by re-scaling the surface heights, we ensure that the synthetic surface topography maps maintain similar surface topography parameters than the experimental surface topography maps.

Previous work (e.g. Refs. [31, 35, 38]) has documented mathematical or statistical approaches to numerically generate surface topography maps that replicate those of machined surfaces. For instance, fractal methods [31] can generate isotropic surface topography patterns of engineering surfaces by utilizing power functions and fractal dimension coefficients. Other mathematical approaches [35, 38] can create simple asperities or combinations of regular machining patterns and asperities at arbitrary locations on the surface. These patterns can be formulated using mathematical functions such as exponential or trigonometric functions. However, generating synthetic LPBF surface topography presents additional challenges compared to numerically generating surface topography that results from machining operations, due to the presence of complex geometric features that occur randomly across the entire surface, including partially melted particles, balling, pores, and laser scan lines.

The nonlinearity and randomness of these geometric patterns and features require highly complicated mathematical equations, which have proven difficult to develop [42]. In contrast, GAN models offer a promising solution to this problem because they identify and generate any complex surface topography map, thus providing a powerful tool to numerically generate synthetic surface topography maps, and reduce the experimental burden to perform intricate surface topography measurements. The results documented by Eastwood et al. [43] primarily focus on augmenting large-scale surface topography maps that result from EBPBF, including top-, up-, and down-skin surfaces. In contrast, this work delves into the specific local geometric features present on as-built

LPBF surfaces, and are crucial to the functionality of the LPBF part.

3.3 Limitations

Despite substantial improvement compared to the state-of-the-art, limitations still exist. First, the method and model are data-oriented, and thus it needs experimental training data as input, which one must obtain through intricate surface topography measurements that require trained personnel. The accuracy of the surface topography measurements also affects the accuracy of the synthetic surface topography maps. Furthermore, it limits the ability to achieve results beyond the scope of the input data, i.e., the model can only recreate features and characteristics that are explicitly part of the experimental surface topography maps that serve as training data for the model.

Second, the optimized generators resulting from the PGGAN model generate synthetic surface topography maps that mostly mimic the experimental surface topography maps and its distinct characteristics and geometric features. Variation exists between individual synthetic surfaces, and some outliers do not show the distinct LPBF surface topography characteristics, which must be considered when using the synthetic surface topography. Moreover, these variations and outliers can lead to statistical differences [56] when comparing surface topography parameters of synthetic and experimental surfaces. Appendix B presents instances of normalized synthetic surface topography maps that successfully capture, and fail to capture the geometric features of the experimental surfaces. Another important limitation is the significant amount of time required to train the PGGAN model, which in this study with a dataset of 18,000 experimental samples took nearly 70 hours.

We also emphasize that we evaluated synthetic surface topography maps using surface topography parameters. However, in computer vision, metrics such as inception score (IS) [57] and Fréchet inception distance (FID) [58] are commonly used to evaluate the quality of generated synthetic images, as they provide a more general evaluation based on feature distance algorithms. Incorporating these metrics could further enhance the generality and accuracy of the

evaluation of synthetic surfaces generated using the GAN model.

4 Conclusions

We present a method to synthetically generate surface topography maps that mimic the surface topography of as-built LPBF surfaces.

1) This work introduces a novel approach to generate synthetic surface topography maps using the PGGAN model. In contrast to previous techniques that rely on mathematical methods such as random surface generation, deterministic surface modeling, or mixed surface approaches, the PGGAN model represents a data-driven approach. It offers advantages in capturing complex surface characteristics and patterns by learning from existing experimental surface topography maps.

2) The PGGAN model successfully generates as-built LPBF surface topography maps that include its typical characteristics and geometric features, such as partially melted particles, pores, laser scan lines, and the balling effect, as evidenced by qualitative comparison of the synthetic and experimental surface topography maps, in addition to a quantitative comparison of areal and deterministic surface topography parameters, radially averaged PSD, and materials ratio curve M_r .

3) Generating synthetic surface topography maps to augment experimental datasets reduces the cost associated with traditional surface topography measurements. The increased data availability also facilitates an improved understanding of the relationship between as-built surface topography and LPBF process parameters, and enables the development of digital twins or data-driven models for complex end-use LPBF parts.

Acknowledgements

Junhyeon SEO and Bart RAEYMAEKERS acknowledge support from the United States Department of Defense, Office of Local Defense Community Cooperation, under award ST1605-21-04. Prahalada RAO acknowledges funding from the United States National Science Foundation (NSF) via Grant numbers: CMMI-2309483

and PFI-TT 2322322. The authors acknowledge Advanced Research Computing at Virginia Tech, USA, for providing computational resources and technical support that have contributed to the results reported within this paper. URL: [https:// arc.vt.edu/](https://arc.vt.edu/)

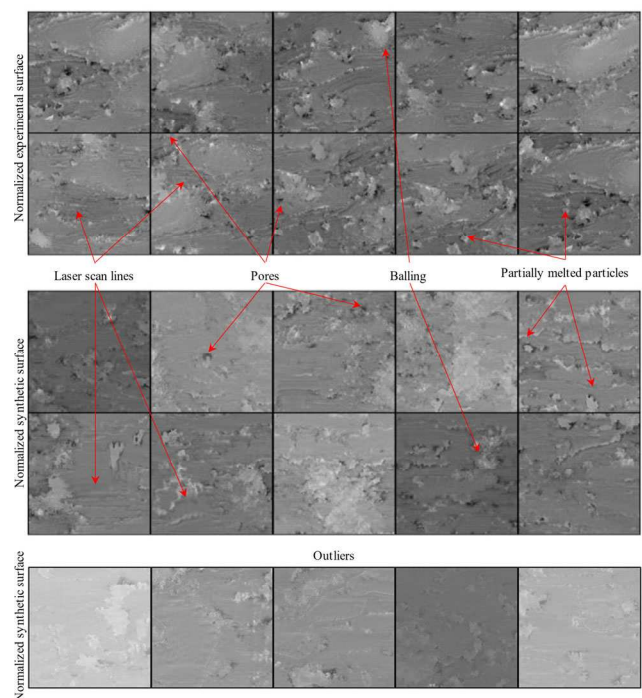
Appendix A

LPBF process parameters for each LPBF specimen.

Specimen number	Contour laser power (W)	Bulk laser power (W)	Laser scan speed (mm/s)	Layer thickness (μm)	Energy density (J/mm^3)
1	115	115	620	30	61.83
2	115	115	620	30	61.83
3	115	168	1,180	30	47.46
4	115	200	800	30	83.33
5	115	220	1,180	30	62.15
6	165	200	1,000	60	50.00

Appendix B

512 pixels x 512 pixels examples of normalized experimental and synthetic surface topography maps with and without (outliers) geometric features of as-built LPBF experimental surfaces.



Data availability

Data generation and ML model development were performed in a Python environment. The relevant codes and data are available on GitHub: https://github.com/junhseo/Friction_J_LPBF_Syn_Gen.git

Declaration of competing interest

The authors have no competing interests to declare that are relevant to the content of this article.

Open Access This article is licensed under a Creative Commons Attribution 4.0 International License, which permits use, sharing, adaptation, distribution and reproduction in any medium or format, as long as you give appropriate credit to the original author(s) and the source, provide a link to the Creative Commons licence, and indicate if changes were made.

The images or other third party material in this article are included in the article's Creative Commons licence, unless indicated otherwise in a credit line to the material. If material is not included in the article's Creative Commons licence and your intended use is not permitted by statutory regulation or exceeds the permitted use, you will need to obtain permission directly from the copyright holder.

To view a copy of this licence, visit <http://creativecommons.org/licenses/by/4.0/>.

References

- [1] Gibson I, Rosen D, Stucker B, Khorasani M, Rosen D, Stucker B, Khorasani M. *Additive Manufacturing Technologies*. Springer New York, New York, 2021.
- [2] Blakey-Milner B, Gradl P, Snedden G, Brooks M, Pitot J, Lopez E, Leary M, Berto F, du Plessis A. Metal additive manufacturing in aerospace: A review. *Mater Des* **209**: 110008 (2021)
- [3] Kerstens F, Cervone A, Gradl P. End to end process evaluation for additively manufactured liquid rocket engine thrust chambers. *Acta Astronaut* **182**: 454–465 (2021)
- [4] Snyder J C, Thole K A. Effect of additive manufacturing process parameters on turbine cooling. *J Turbomach* **142**(5): 051007 (2020)
- [5] Leal R, Barreiros F M, Alves L, Romeiro F, Vasco J C, Santos M, Marto C. Additive manufacturing tooling for the automotive industry. *Int J Adv Manuf Technol* **92**(5–8): 1671–1676 (2017)
- [6] Vasco J C. Additive manufacturing for the automotive industry. In: *Additive Manufacturing*. Amsterdam: Elsevier: 505–530, 2021
- [7] Singh S, Ramakrishna S. Biomedical applications of additive manufacturing: Present and future. *Curr Opin Biomed Eng* **2**: 105–115 (2017)
- [8] Puppi D, Chiellini F. Biodegradable polymers for biomedical additive manufacturing. *Appl Mater Today* **20**: 100700 (2020)
- [9] Murr L E, Gaytan S M, Medina F, Lopez H, Martinez E, Machado B I, Hernandez D H, Martinez L, Lopez M I, Wicker R B, et al. Next-generation biomedical implants using additive manufacturing of complex, cellular and functional mesh arrays. *Philos Trans A Math Phys Eng Sci* **368**(1917): 1999–2032 (2010)
- [10] Kumbhar N N, Mulay A V. Post processing methods used to improve surface finish of products which are manufactured by additive manufacturing technologies: A review. *J Inst Eng Ind Ser C* **99**(4): 481–487 (2018)
- [11] Carter L N, Martin C, Withers P J, Attallah M M. The influence of the laser scan strategy on grain structure and cracking behaviour in SLM powder-bed fabricated nickel superalloy. *J Alloys Compd* **615**: 338–347 (2014)
- [12] Jiang R B, Mostafaei A, Pauza J, Kantzos C, Rollett A D. Varied heat treatments and properties of laser powder bed printed Inconel 718. *Mater Sci Eng A* **755**: 170–180 (2019)
- [13] Newell D J, O'Hara R P, Cobb G R, Palazotto A N, Kirka M M, Burggraf L W, Hess J A. Mitigation of scan strategy effects and material anisotropy through supersolvus annealing in LPBF IN₇₁₈. *Mater Sci Eng A* **764**: 138230 (2019)
- [14] Lee S C, Chang S H, Tang T P, Ho H H, Chen J K. Improvement in the microstructure and tensile properties of inconel 718 superalloy by HIP treatment. *Mater Trans* **47**(11): 2877–2881 (2006)
- [15] Tian Z H, Zhang C Q, Wang D Y, Liu W, Fang X Y, Wellmann D, Zhao Y T, Tian Y T. A review on laser powder bed fusion of inconel 625 nickel-based alloy. *Appl Sci* **10**(1): 81 (2019)
- [16] Mohammadian N, Turenne S, Brailovski V. Surface finish control of additively-manufactured Inconel 625 components using combined chemical-abrasive flow polishing. *J Mater Process Technol* **252**: 728–738 (2018)
- [17] Pyka G, Kerckhofs G, Papantoniou I, Speirs M, Schrooten J, Wevers M. Surface roughness and morphology customization of additive manufactured open porous Ti₆Al₄V structures. *Materials* **6**(10): 4737–4757 (2013)
- [18] Calignano F, Manfredi D, Ambrosio E P, Iuliano L, Fino P. Influence of process parameters on surface roughness of

- aluminum parts produced by DMLS. *Int J Adv Manuf Technol* **67**(9–12): 2743–2751 (2013)
- [19] Lesyk D A, Martinez S, Mordiyuk B N, Dzhemelinskyi V V, Lamikiz, Prokopenko G I. Post-processing of the Inconel 718 alloy parts fabricated by selective laser melting: Effects of mechanical surface treatments on surface topography, porosity, hardness and residual stress. *Surf Coat Technol* **381**: 125136 (2020)
- [20] Özel T, Altay A, Kaftanoğlu B, Leach R, Senin N, Donmez A. Focus variation measurement and prediction of surface texture parameters using machine learning in laser powder bed fusion. *J Manuf Sci Eng* **142**(1): 011008 (2020)
- [21] Raeymaekers B, Talke F E. The effect of laser polishing on fretting wear between a hemisphere and a flat plate. *Wear* **268**(5–6): 416–423 (2010)
- [22] ISO. ISO 21920-2:2021. Geometrical product specifications (GPS)—Surface texture: Areal—Part 2: Terms, definitions, and surface texture parameters. International Organization for Standardization, 2012.
- [23] Detwiler S, Watring D, Spear A, Raeymaekers B. Relating the surface topography of as-built Inconel 718 surfaces to laser powder bed fusion process parameters using multivariate regression analysis. *Precis Eng* **74**: 303–315 (2022)
- [24] Detwiler S, Raeymaekers B. Deriving data-driven models that relate deterministic surface topography parameters of as-built Inconel 718 surfaces to laser powder bed fusion process parameters. *J Tribol* **144**(12): 121703 (2022)
- [25] Elambasseril J, Rogers J, Wallbrink C, Munk D, Leary M, Qian M. Laser powder bed fusion additive manufacturing (LPBF-AM): The influence of design features and LPBF variables on surface topography and effect on fatigue properties. *Crit Rev Solid State Mater Sci* **48**(1): 132–168 (2023)
- [26] Watring D S, Carter K C, Crouse D, Raeymaekers B, Spear A D. Mechanisms driving high-cycle fatigue life of as-built Inconel 718 processed by laser powder bed fusion. *Mater Sci Eng A* **761**: 137993 (2019)
- [27] Raeymaekers B. *Design of Mechanical Elements: A Concise Introduction to Mechanical Design Considerations and Calculations*. John Wiley & Sons, 2022.
- [28] Leach R K. *Fundamental principles of engineering nanometrology*. Elsevier, 2010.
- [29] Whitehouse D J. *Handbook of Surface Metrology*. CRC Press, 1994.
- [30] Pawlus P, Reizer R, Wieczorowski M. A review of methods of random surface topography modeling. *Tribol Int* **152**: 106530 (2020)
- [31] Ganti S, Bhushan B. Generalized fractal analysis and its applications to engineering surfaces. *Wear* **180**(1–2): 17–34 (1995)
- [32] Majumdar A, Bhushan B. Role of fractal geometry in roughness characterization and contact mechanics of surfaces. *J Tribol* **112**(2): 205–216 (1990)
- [33] Majumdar A, Bhushan B. Fractal model of elastic-plastic contact between rough surfaces. *J Tribol* **113**(1): 1–11 (1991)
- [34] Persson B N J. On the fractal dimension of rough surfaces. *Tribol Lett* **54**(1): 99–106 (2014)
- [35] Francis H A. A finite surface element model for plane-strain elastic contact. *Wear* **76**(2): 221–245 (1982)
- [36] Megalingam A, Mayuram M M. Comparative contact analysis study of finite element method based deterministic, simplified multi-asperity and modified statistical contact models. *J Tribol* **134**(1): 1 (2012)
- [37] Pasaribu H R, Schipper D J. Application of a deterministic contact model to analyze the contact of a rough surface against a flat layered surface. *J Tribol* **127**(2): 451–455 (2005)
- [38] Francisco A, Brunetière N. A hybrid method for fast and efficient rough surface generation. *Proc Inst Mech Eng Part J J Eng Tribol* **230**(7): 747–768 (2016)
- [39] Lou S, Jiang X, Sun W, Zeng W, Pagani L, Scott P J. Characterisation methods for powder bed fusion processed surface topography. *Precis Eng* **57**: 1–15 (2019)
- [40] Townsend A, Senin N, Blunt L, Leach R K, Taylor J S. Surface texture metrology for metal additive manufacturing: A review. *Precis Eng* **46**: 34–47 (2016)
- [41] Goodfellow I, Pouget-Abadie J, Mirza M, Xu B, Warde-Farley D, Ozair S, Courville A, Bengio Y. Generative adversarial networks. *Commun ACM* **63**(11): 139–144 (2020)
- [42] Karras T, Aila T M, Laine S, Lehtinen J. Progressive growing of GANs for improved quality, stability, and variation. arXiv: 1710.10196. (2017)
- [43] Eastwood J, Newton L, Leach R, Piano S. Generation and categorisation of surface texture data using a modified progressively growing adversarial network. *Precis Eng* **74**: 1–11 (2022)
- [44] Watring D S, Benzing J T, Hrabe N, Spear A D. Effects of laser-energy density and build orientation on the structure-property relationships in as-built Inconel 718 manufactured by laser powder bed fusion. *Addit Manuf* **36**: 10.1016/j.addma.2020.101425 (2020)
- [45] Al-Maharma A Y, Patil S P, Markert B. Effects of porosity on the mechanical properties of additively manufactured components: A critical review. *Mater Res Express* **7**(12): 122001 (2020)
- [46] Du Plessis A, Yadroitsava I, Yadroitsev I. Effects of defects on mechanical properties in metal additive manufacturing: A review focusing on X-ray tomography insights. *Mater Des* **187**: 108385 (2020)

- [47] Kim F H, Kim F H, Moylan S P. Literature review of metal additive manufacturing defects, Advanced Manufacturing Series (NIST AMS), National Institute of Standards and Technology, Gaithersburg, USA, 2018: <https://doi.org/10.6028/NIST.AMS.100-16>.
- [48] Maleki E, Bagherifard S, Bandini M, Guagliano M. Surface post-treatments for metal additive manufacturing: Progress, challenges, and opportunities. *Addit Manuf* **37**: 101619 (2021)
- [49] Li R D, Liu J H, Shi Y S, Wang L, Jiang W. Balling behavior of stainless steel and nickel powder during selective laser melting process. *Int J Adv Manuf Technol* **59**(9–12): 1025–1035 (2012)
- [50] Reijonen J, Revuelta A, Riipinen T, Ruusuvoori K, Puukko P. On the effect of shielding gas flow on porosity and melt pool geometry in laser powder bed fusion additive manufacturing. *Addit Manuf* **32**: 101030 (2020)
- [51] Leary M. (2017) Surface roughness optimisation for selective laser melting (SLM): Accommodating relevant and irrelevant surfaces. In: *Laser Additive Manufacturing*, Elsevier, 2017: 99–118.
- [52] Yasa E, Poyraz O, Solakoglu E U, Akbulut G, Oren S. A study on the stair stepping effect in direct metal laser sintering of a nickel-based superalloy. *Procedia CIRP* **45**: 175–178 (2016)
- [53] Mahboob Kanafi M, Tuononen A J. Top topography surface roughness power spectrum for pavement friction evaluation. *Tribol Int* **107**: 240–249 (2017)
- [54] Kalin M, Pogačnik A, Etsion I, Raeymaekers B. Comparing surface topography parameters of rough surfaces obtained with spectral moments and deterministic methods. *Tribol Int* **93**: 137–141 (2016)
- [55] Pawar G, Pawlus P, Etsion I, Raeymaekers B. The effect of determining topography parameters on analyzing elastic contact between isotropic rough surfaces. *J Tribol* **135**(1): 011401 (2013)
- [56] Kim T K. T test as a parametric statistic. *Korean J Anesthesiol* **68**(6): 540 (2015)
- [57] Barratt S, Sharma R. A note on the inception score. *arXiv preprint*: arXiv: 1801.01973 (2018)
- [58] Heusel M, Ramsauer H, Unterthiner T, Nessler B, Hochreiter S. (2017) GANs trained by a two time-scale update rule converge to a local Nash equilibrium. In: Proceedings of the 31st International Conference on Neural Information Processing Systems. New York, 2017: 6629–6640.



Junhyeon SEO. He received his Ph.D. in ocean and aerospace engineering from Virginia Tech, USA, in 2022.

He was a post-doctoral associate until Oct. 2023, and currently is a research scientist at the National Aeronautics and Space Administration (NASA), USA.



Prahalada RAO. He received his Ph.D. degree in industrial engineering from the Oklahoma State University, USA, in 2013. He

is currently an associate professor in the Grado Department of Industrial and Systems Engineering at Virginia Tech in Blacksburg, USA.



Bart RAEYMAEKERS. He received his Ph.D. in mechanical engineering from the University of California

San Diego, USA, in 2007. He currently is a professor of mechanical engineering at Virginia Tech in Blacksburg, USA.